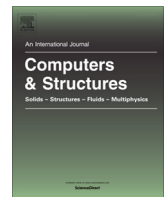




ELSEVIER

Contents lists available at ScienceDirect

# Computers and Structures

journal homepage: [www.elsevier.com/locate/compstruc](http://www.elsevier.com/locate/compstruc)

## Improvement of size effect simulation based on an energy-balanced exponential softening bond model and fracture energy regularization

Tao Wang, Huai-Zhong Liu <sup>\*</sup>, Ming-Li Xiao, Li Zhuo, Hong-Qiang Xie, Jiang-Da He

State Key Laboratory of Hydraulics and Mountain River Engineering, College of Water Resources and Hydropower, Sichuan University, Chengdu 610065, Sichuan, China

### ARTICLE INFO

**Article history:**

Received 23 October 2022

Accepted 12 February 2023

Available online 4 March 2023

**Keywords:**

Size effect

Exponential softening

Contact model

Three-point bending

Discrete element method

### ABSTRACT

Although the Mode I fracture of rock demonstrates a noticeable size effect, current contact models in the discrete element method cannot simulate the size effect very well. An exponential softening bond model is proposed to address this issue based on an exponential damage law and an elliptic yield criterion. Its basic formulas are established on energy balance to ensure that the total fracture energy of the normal and shear springs always equals the fracture energy dissipated by the resultant contact force. The simulations of uniaxial tensile and three-point bending tests were conducted to demonstrate the performances of the proposed model on the fracture simulations. The particle size dependency is successfully eliminated by fracture energy regularization, in which the force-displacement relationship is adjusted based on fracture energy and particle size. The simulation results show that the exponential softening bond model effectively simulates the whole load-displacement curves of experimental tests. It also demonstrates a perfect energy balance among external work, internal energy, and fracture energy. Besides, compared with the other two bond models, the exponential softening bond model is more precise in representing the fracture toughness, the fracture process zone, and the size effect of the Mode I fracture of limestone.

© 2023 Elsevier Ltd. All rights reserved.

### 1. Introduction

Many engineering challenges have become more complex in recent years because of the scale expansion of underground constructions, such as underground caverns of hydropower stations, traffic tunnels, mines, and shale gas exploitations. Engineers are paying more and more attention to fracture problems of surrounding rock, such as rock bursts and spalling failures caused by underground excavation. To reasonably assess the stability of surrounding rock, it is necessary to obtain the proper mechanical parameters of rock mass at an engineering scale. However, numerous studies show that some mechanical properties, such as fracture toughness, compressive strength, and tensile strength, exhibit pronounced size effects and decrease as structural size increases [1–3]. Thus, the size effect must be considered when performing a numerical simulation of rock material.

The existence of randomly distributed flaws, such as pores and microcracks, is the primary cause of the size effect. The increasing rock size increases the number of flaws and the probability of large-scale flaws. As a result, the rock's macroscopic strength

decreases. Therefore, early studies concentrated on the linear elastic fracture mechanics and the strength distribution theories, such as Griffith's strength theory [4] and Weibull distribution theory [5]. Meanwhile, the crack would not propagate linearly due to randomly distributed defects. Bažant et al. [6] believe the crack spreads in a band-like pattern and the crack tip has a banded region of strain softening damage. They developed a size effect theory based on the energy dissipation of the crack band.

Hereafter, softening damage models were widely used in the numerical simulations of fracture and size effects. These simulation methods include the finite element method (FEM) and the discrete element method (DEM). Some contact and stress-strain constitutive models in FEM, such as Cohesive Crack Model [7,8] and Continuum Damage Model [9–11], are widely used to simulate the crack propagation process. DEM represents solid material as some randomly distributed and bonded particles and could simulate the microscale fracture behavior of solid materials. Additionally, DEM can be used to simulate the softening damage characteristics of materials by employing softening bond model. Therefore, DEM is widely used to study some strength characteristics and fracture behaviors of geotechnical materials [12–14].

However, no matter which method is adopted to simulate the fracture behavior, element or particle size could affect the simulation results, known as the size dependency of mesh or particle size.

\* Corresponding author.

E-mail address: [huaizhong.liu@scu.edu.cn](mailto:huaizhong.liu@scu.edu.cn) (H.-Z. Liu).

For instance, Potyondy and Cundall [15] analyzed the fracture properties of DEM and established a relationship between model I fracture toughness and DEM parameters. They discovered that the model I fracture toughness is proportional to the square root of particle radius. Consequently, to eliminate the size dependency of mesh (particle size) in the simulation of some nonlinear fracture problems, such as size effect, that are necessary not only to control the element or particle size but also to adjust the softening damage constitutive relation according to the size [16]. The fundamental goal of the adjustment is to maintain consistency in the unit fracture energy dissipated by elements or particles of various sizes. There are some quite mature technologies used in FEM, such as the Gradient enhanced damage model [17], the Nonlocal model [18], and the Phase-field model [19]. However, such technologies need to be developed in DEM.

Another deficiency of DEM is that some widely used contact models cannot represent the nonlinear size effect of fracture. The contact bond model and the parallel bond model are two popular models, and both of them are brittle bonds, which means that they break when the contact tensile (or shear) force is greater than the bond tensile (or shear) strength. The size effects represented by these models follow linear elastic mechanics [15,20], so they cannot describe the size effect of nonlinear rock strength. Inspired by the finite element softening damage model, some softening bond models have also been developed in DEM, but these models are linear softening models [21–24]. Kim et al. [22,23] simulated the fracture behavior of asphalt concrete under compact tension test introducing an intrinsic linear softening model in PFC<sup>2D</sup>, but they did not study the nonlinear fracture properties of quasi-brittle materials. Fakhimi and Tarokh [24] simulated the size effect of rock subjected to three-point bending using the linear softening bond model, and their simulation results match well with the Bažant size effect law. However, the linear softening bond cannot accurately reflect the traction-separation relation of rock fracture, and the simulated load-deformation curves deviate significantly from the test results.

This study develops an energy-balanced exponential softening bond model based on PFC<sup>2D</sup> to simulate the size effect of Mode I fracture of brittle materials. First, the model's constitutive equations, the yield criterion, the realization of progressive softening, and the elimination method of particle size dependency were presented in detail. Second, the simulated load-deformation relations and fracture energies of a single contact and a uniaxial tensile test were analyzed to illustrate the validity and performance of the proposed model on nonlinear fracture analysis. Third, the simulations of three-point bending fracture tests of limestone were carried out by three different contact models to demonstrate the capacity of the proposed model on the size effect of Mode I fracture.

## 2. The exponential softening bond model

### 2.1. Elastic constitutive relations of contact in any direction

In DEM, most constitutive models transmit only forces between two particles by the normal and shear springs, such as the contact bond model. Some constitutive models transmit not only forces but also moment by bond, such as the parallel bond model. Because the moment could make the secondary development process more complex, the exponential softening bond model is developed based on the contact bond model. The contact bond model assumes that the constitutive relations of normal and shear springs are mutually independent. The separated constitutive relations cannot demonstrate the interaction mechanism between normal and shear strengths. Therefore, it's necessary to unify the deformation behaviors of normal and shear springs into an elastic constitu-

tive relation before introducing the exponential softening bond model.

As shown in Fig. 1(a), the contact bond model consists of normal and shear springs. Their contact force and displacement relationships are controlled by the normal stiffness and shear stiffness, respectively, and expressed as  $F_n = K_n u_n$  and  $F_s = K_s u_s$ . The resultant contact force is:

$$F_\alpha = \sqrt{F_n^2 + F_s^2} \quad (1)$$

where  $F_n$  and  $F_s$  are the normal and shear forces, respectively, and  $u_n$  and  $u_s$  are the normal and shear displacements, respectively.

If the angle between the resultant force and the normal direction is  $\alpha$ , then  $F_n = F_\alpha \cos \alpha$  and  $F_s = F_\alpha \sin \alpha$ . After substituting them into the constitutive relations of two springs, the displacement components can be expressed as  $u_n = F_\alpha \cos \alpha / K_n$  and  $u_s = F_\alpha \sin \alpha / K_s$ . The resultant contact displacement is:

$$u = \sqrt{u_n^2 + u_s^2} = F_\alpha \sqrt{\frac{\cos^2 \alpha}{K_n^2} + \frac{\sin^2 \alpha}{K_s^2}} \quad (2)$$

To achieve a reasonable Poisson's ratio,  $K_n$  is usually not equal to  $K_s$ , so the resultant displacement  $\vec{u}$  and the resultant force  $\vec{F}_\alpha$  are usually not in the same direction, as shown in Fig. 1(b). The angle  $\theta$  between the resultant displacement  $\vec{u}$  and the resultant force  $\vec{F}_\alpha$  can be solved as:

$$\cos \theta = \left( \frac{\cos^2 \alpha}{K_n} + \frac{\sin^2 \alpha}{K_s} \right) / \sqrt{\frac{\cos^2 \alpha}{K_n^2} + \frac{\sin^2 \alpha}{K_s^2}} \quad (3)$$

From the perspective of energy balance, the work done by the resultant force is:

$$W = \int \vec{F}_\alpha d\vec{u} = \int F_\alpha d(u \cos \theta) \quad (4)$$

where  $u \cos \theta$  is the projected displacement in the direction of the resultant force and is expressed as:

$$u_\alpha = u \cos \theta \quad (5)$$

Furthermore, the constitutive relation between contact force and displacement in the direction  $\alpha$  can be expressed as  $C(F_\alpha, u_\alpha)$ . If  $\alpha = 0$ , then  $\theta = 0$ , and  $C(F_\alpha, u_\alpha)$  becomes the constitutive relation of normal spring  $C(F_n, u_n)$ ; if  $\alpha = 90^\circ$ , then  $\theta = 90^\circ$ , and  $C(F_\alpha, u_\alpha)$  becomes the constitutive relation of the shear spring  $C(F_s, u_s)$ . The elastic constitutive relation in the direction  $\alpha$  can be expressed as  $F_\alpha = K_\alpha u_\alpha$ , where  $K_\alpha$  is the equivalent stiffness and can be solved as  $K_\alpha = F_\alpha / (u \cos \theta)$ . Substituting Eqs (1)–(3) into it generates:

$$K_\alpha = 1 / \left( \frac{\cos^2 \alpha}{K_n} + \frac{\sin^2 \alpha}{K_s} \right) \quad (6)$$

Eq. (4) shows that the elastic constitutive relation in the direction  $\alpha$  is based on energy balance, so the strain energy obtained from the relation  $C(F_\alpha, u_\alpha)$  in any direction is always equal to the sum of strain energies obtained from the normal and shear springs, as verified in the following section.

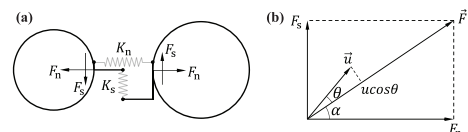


**Fig. 1.** Relation between force and displacement of the contact model. (a) Schematic diagram of the contact model. (b) The relation between the resultant force and the resultant displacement.

## 2.2. Yield criterion and the exponential softening bond model

The contact bond model is a brittle bond. The bond breaks either when the normal force is greater than the tensile strength or when the shear force is greater than the shear strength, and only the residual contact friction effect remains after it breaks. The corresponding yield criterion is shown as the dashed line in Fig. 2(a). The shear strength of contact increases under the action of normal compression, while it's unaffected by normal tension. However, Nooru-Mohamed [25] conducted various loading tests on double-edge notched samples, and the experimental results show that the maximum attainable shear loads were reduced by the damage caused by the tension load. Therefore, the proposed model maintains the Mohr-Coulomb criterion in the compression region and improves the yield criterion with an elliptical yield criterion in the tension region. The improved yield criterion is expressed as:

$$\begin{cases} F_n^2/S_n^2 + F_s^2/S_s^2 = 1 & , F_n \leq 0 \\ F_s = S_s + \mu F_n & , F_n > 0 \end{cases} \quad (7)$$

where  $S_n$  and  $S_s$  are the tensile and shear strength, respectively,  $\mu$  is the friction coefficient and  $\mu = \tan \varphi$ , and  $\varphi$  is the friction angle.

According to the elliptical yield criterion, the contact strength in the direction of  $\alpha$  can be determined as:

$$S_\alpha = \frac{S_n S_s}{\sqrt{S_n^2 \sin^2 \alpha + S_s^2 \cos^2 \alpha}} \quad (8)$$

Similarly,  $S_n$  and  $S_s$  are two special cases of  $S_\alpha$ . After the applied force reaches the initial yield surface, the proposed softening bond will turn into a softening stage, and its bearing capacity will gradually decrease. The softening bond breaks when the contact force reaches zero. As shown in Fig. 2(b), the softening process is characterized by a gradual shift of the yield surface, and it can be mathematically described by a single damage variable  $D_f$  [26]. Based on the exponential damage law proposed by Jirásek and Bauer [16], the  $D_f$  is defined as:

$$D_f = \begin{cases} 0 & , u_\alpha \leq u_{\alpha e} \\ 1 - \frac{u_{\alpha e}}{u_\alpha} \exp \left( -\frac{u_\alpha - u_{\alpha e}}{u_{\alpha f} - u_{\alpha e}} \right) & , u_\alpha > u_{\alpha e} \end{cases} \quad (9)$$

where  $u_{\alpha e}$  is the elastic limit displacement expressed as  $u_{\alpha e} = S_\alpha / K_\alpha$ , and  $u_{\alpha f}$  is an exponential damage parameter that controls the shape of softened strength curve as shown in Fig. 3. The softened strength is determined as:

$$S_{\alpha,sof} = (1 - D_f) K_\alpha u_\alpha = S_\alpha \exp \left( -\frac{u_\alpha - u_{\alpha e}}{u_{\alpha f} - u_{\alpha e}} \right) \quad (10)$$

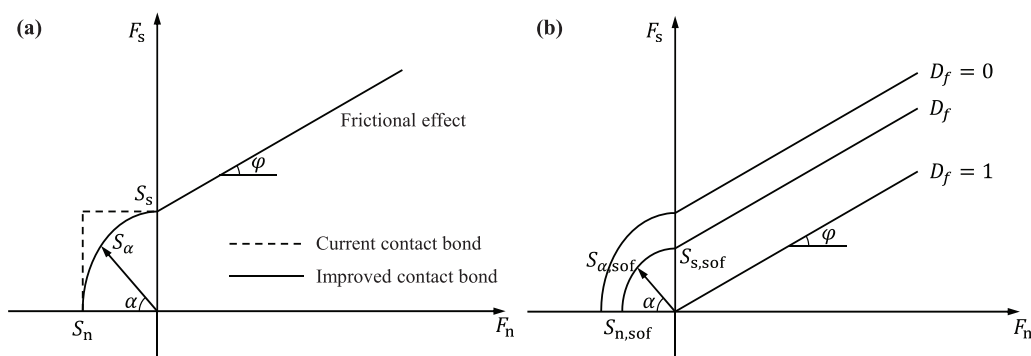


Fig. 2. Yield criterion of the exponential softening bond model. (a) Initial yield surface and (b) softening yield surface.

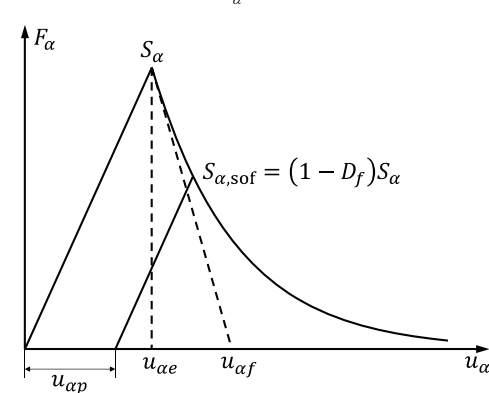


Fig. 3. Load-displacement curve of the exponential softening bond model.

Then the tensile strength of the normal spring and the shear strength of the shear spring are also determined as  $S_{n,sof} = S_n \exp \left( -\frac{u_n - u_{ne}}{u_{nf} - u_{ne}} \right)$  and  $S_{s,sof} = S_s \exp \left( -\frac{u_s - u_{se}}{u_{sf} - u_{se}} \right)$ , respectively. As shown in Fig. 3, the plastic deformation after unloading is solved as:

$$u_{zp} = u_\alpha - \frac{S_{\alpha,sof}}{K_\alpha} = u_\alpha - (1 - D_f) u_{ze} \quad (11)$$

## 2.3. Fracture energy regularization

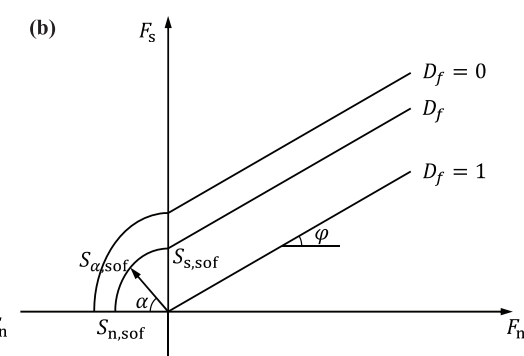
Fracture energy is a crucial component in fracture mechanics and is directly related to the evaluation of fracture toughness. It is defined as the energy released when a crack propagates unit area, so it equals the total energy released divided by the bond area when a bond breaks, namely:

$$g_f = \frac{1}{2Rt} \int_0^\infty F_\alpha(u_\alpha) du_\alpha = \frac{S_\alpha}{2Rt} \left( u_{zf} - \frac{S_\alpha}{2K_\alpha} \right) \quad (12)$$

where  $\bar{R}$  is the bond radius, which equals the average radius of two contacted particles, and  $t$  is the thickness of discs. If the contact strength and displacements in the equation are expressed as  $S_\alpha = 2\bar{R}\sigma_\alpha$ ,  $u_{zf} = 2\bar{R}\varepsilon_{zf}$ , and  $u_{ze} = S_\alpha/K_\alpha = 2\bar{R}\varepsilon_{ze}$ , the fracture energy can also be expressed as:

$$g_f = \sigma_\alpha \bar{R} (2\varepsilon_{zf} - \varepsilon_{ze}) \quad (13)$$

where  $\varepsilon_{ze}$  and  $\varepsilon_{zf}$  are strains corresponding to the elastic limit and the exponential damage parameter, respectively, and  $\sigma_\alpha$  is the material strength in the direction of  $\alpha$ . This equation shows



that the fracture energy is positively related to the bond radius, which means that the particle radius cannot be chosen arbitrarily in the simulation of material with prescribed fracture energy. Thus, a strategy of fracture energy regularization is introduced to eliminate the particle size dependency. The strategy proposed for the exponential softening model is that the model parameter  $u_{\alpha f}$  is adjusted according to the bond radius of contact and the prescribed fracture energy. From Eq. (12), the variable damage parameter  $u_{\alpha f}$  can be determined as:

$$u_{\alpha f} = \frac{S_\alpha}{2K_\alpha} + \frac{2\bar{R}tg_f}{S_\alpha} \quad (14)$$

The damage parameter  $u_{\alpha f}$  is connected to the bond radius  $\bar{R}$  by this formula. The relation between force and displacement of the bond varies with the bond radius, while the fracture energy of the bond remains constant. Thus, this size dependence of simulation results can be eliminated by the fracture energy regularization.

#### 2.4. Algorithm of progressive softening

The exponential softening bond model was developed in PFC<sup>2D</sup> [27]. The software uses a time-step algorithm and solves the contact force by using the motion increment of the current time step. In response to displacement increments,  $\Delta u_n$  and  $\Delta u_s$ , the normal and shear contact force increments were calculated as  $\Delta F_n = K_n \Delta u_n$  and  $\Delta F_s = K_s \Delta u_s$ . By adding them to the original contact force,  $F_n^{i-1}$  and  $F_s^{i-1}$ , the trial forces are obtained as  $F_n^i$  and  $F_s^i$ . If the force state  $(F_n^i, F_s^i)$  is within the yield surface determined by damage variable  $D_f^{i-1}$ , all the increments are elastic, and the trial contact forces are the new ones,  $F_n^i$  and  $F_s^i$ . Otherwise, a part of displacement is plastic, and the new contact forces are determined according to the following plastic flow law. The linear displacement softening model included in PFC<sup>2D</sup> specifies the following plastic flow law. When  $F_n^i \leq 0$ , plastic displacement increment  $\Delta u_{ap}$  is in the direction of the resultant force  $\vec{F}_\alpha^i(F_n^i, F_s^i)$ , so the direction of the resultant force remains unchanged after softening. When  $F_n^i > 0$ , plastic displacement increment  $\Delta u_{sp}$  is in the direction of the shear force, and the normal force remains unchanged. The exponential softening bond model follows the above plastic flow law, as shown in Fig. 4. Although the direction of shear and tensile-shear plastic flow are different, the update processes of shear and tensile-shear forces after softening are similar. The update of tensile-shear force is illustrated in Fig. 5. The shear force is updated by replacing  $u_\alpha$  and  $F_\alpha$  with  $u_s$  and  $F_s - \mu F_n$  on the horizontal and vertical axes, respectively. Only the formulas of tensile-shear softened force are presented here to avoid repetition. The

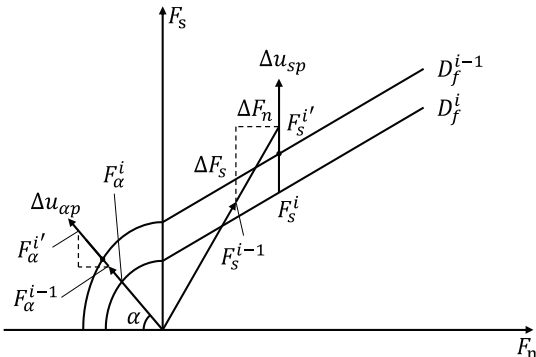


Fig. 4. Sketch of the direction of plastic displacement increment.

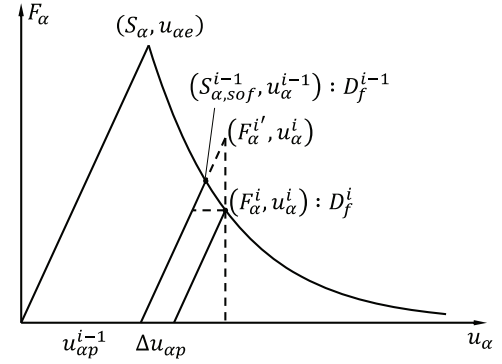


Fig. 5. Interpretation of plastic displacement increment.

related update of plastic displacement increment  $\Delta u_{ap}$  and damage variable  $D_f^i$  are also elaborated.

The current damage variable  $D_f^i$ , softened strength  $S_{\alpha,sof}^i$ , and plastic displacement  $u_{\alpha p}^i$  of the contact can be uniquely determined by the displacement  $u_\alpha^i$ , as shown in Fig. 5. However, PFC<sup>2D</sup> uses an algorithm of displacement increments in kernel computation and the displacement  $u_\alpha^i$  cannot be obtained directly. Besides, the displacement condition of contact isn't always on the strength curve when subjected to complex loads. Thus, the previous displacement state  $u_\alpha^{i-1}$  needs to be inversely solved by the previous damage variable  $D_f^{i-1}$ . The damage function  $D_f(u_\alpha)$  is a monotonically increasing function indicated by Eq. (9). If the damage variable  $D_f$  is known, the corresponding displacement  $u_\alpha$  can be uniquely determined. However, it is difficult to obtain the explicit expression of the inverse function  $u_\alpha(D_f)$ . Therefore, the Newton-Raphson method was used to solve the displacement:

$$u_\alpha^{n+1} = u_\alpha^n - \frac{D_f(u_\alpha^n) - D_f^{i-1}}{D_f'(u_\alpha^n)}, \quad u_\alpha^0 = u_{\alpha e} \quad (15)$$

where the superscript  $n$  indicates the iterative number of the Newton-Raphson method, and the superscript  $i$  indicates the time-step in PFC<sup>2D</sup>. The Newton-Raphson method has the characteristics of high computational efficiency and fast convergency. If the elastic limit displacement is taken as the initial value, the number of iterations for different damage variables is shown in Fig. 6. The number of iterations gradually increases as the damage variable increases. The displacement error could decrease to a tolerance of  $10^{-6}$  μm within ten iterations.

After  $u_\alpha^{i-1}$  is solved, the previous yield strength can be determined as  $S_{\alpha,sof}^{i-1} = (1 - D_f^{i-1})K_\alpha u_\alpha^{i-1}$  according to Eq. (10), and the

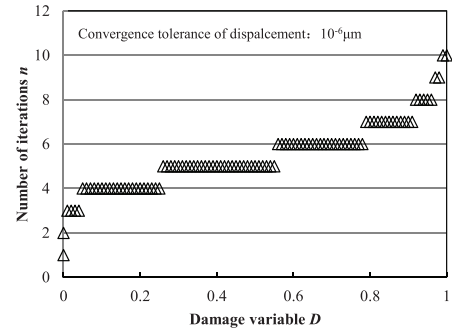


Fig. 6. The convergence analysis of Newton-Raphson iteration used to solve the current displacement.

previous plastic displacement can be determined as  $u_{zp}^{i-1} = D_f^{i-1} u_z^{i-1}$  according to Eq. (11). When the trial resultant force  $F_\alpha^i$  is greater than  $S_{\alpha,sof}^{i-1}$ , the current contact displacement is calculated as:

$$u_z^i = u_{zp}^{i-1} + \frac{F_\alpha^i}{K_\alpha} \quad (16)$$

The current damage variable  $D_f^i$ , softened resultant force  $F_\alpha^i$ , and plastic displacement increment  $\Delta u_{zp}$  can be determined by substituting  $u_z^i$  into Eqs. (9)-(11). Then, the softened normal force  $F_n^i$  and shear force  $F_s^i$  are determined as:

$$F_n^i = \frac{F_n^i}{F_\alpha^i} F_\alpha^i, \quad F_s^i = \frac{F_s^i}{F_\alpha^i} F_\alpha^i \quad (17)$$

### 3. Model verification based on analyses of fracture energy

#### 3.1. Characteristic of fracture energy balance

According to the principle that the contact force vector does work in the direction of the displacement vector, after a bond is

broken, the fracture energy done by the resultant force should be equal to the sum of the fracture energies released by the normal and shear springs and should also be consistent with the fracture energy prescribed by the input parameter. To verify whether the simulated contact force-displacement curve is consistent with the theoretical solution and to check the fracture energy balance, a single contact formed by two disks was simulated. The radii of two disks  $R$  are 5 mm, and other contact parameters are  $K_n = 33$  GPa,  $K_s = 16.5$  GPa,  $S_n = 35$  kN,  $S_s = 35$  kN,  $\mu = 0.5$ , and  $g_f = 25$  N/m. The loading direction  $\alpha$  is taken as  $0^\circ, 30^\circ, 45^\circ, 60^\circ$ , and  $90^\circ$ , respectively. When  $\alpha = 30^\circ$ , the curve of  $F_\alpha$  versus  $u_\alpha$  is shown in Fig. 7(a). The simulation result matches the theoretical solution very well, so the algorithm of the proposed model is accurate. The resultant fracture energy,  $g_\alpha$ , done by the resultant force equals the enclosed area surrounded by the  $F_\alpha$ - $u_\alpha$  curve and the  $u_\alpha$  axis divided by the contact area  $2Rt$ . The simulated  $F_n$ - $u_n$  curve and  $F_s$ - $u_s$  curve are shown in Fig. 7(b) and 7(c), respectively. Similarly, the normal fracture energy,  $g_n$ , and the shear fracture energy,  $g_s$ , can be determined by the respective enclosed area divided by  $2Rt$ . The fracture energy results of various loading directions are listed in Table 1. No matter which loading direction, the sum of the normal fracture energy and shear fracture energy is always

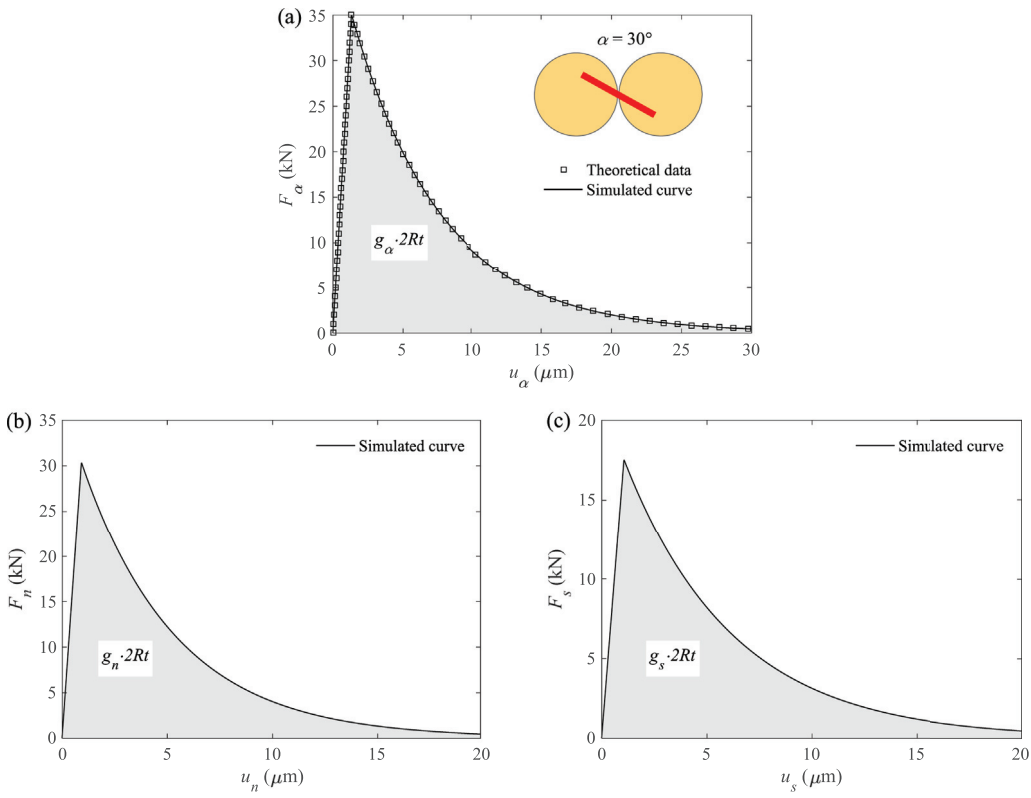


**Fig. 7.** Contact force-displacement curves simulated by the exponential softening bond model. (a) Curve of  $F_\alpha$ - $u_\alpha$ , (b) curve of  $F_n$ - $u_n$ , and (c) curve of  $F_s$ - $u_s$ .

**Table 1**  
Analysis of fracture energy.

Loading direction $\alpha(^{\circ})$	Normal fracture energy $g_n(\text{N}/\text{m})$	Shear fracture energy $g_s(\text{N}/\text{m})$	$g_n + g_s$ ( $\text{N}/\text{m}$ )	Resultant fracture energy $g_\alpha(\text{N}/\text{m})$	Prescribed fracture energy $g_f(\text{N}/\text{m})$
0	25.00	0.00	25.00	25.00	25
30	14.99	10.00	24.99	24.99	
45	8.33	16.66	24.99	24.99	
60	3.57	21.42	24.99	24.99	
90	0.00	25.00	25.00	25.00	

equal to the resultant fracture energy and the prescribed fracture energy, so the fracture energy balance is also verified.

### 3.2. Fracture energy analysis of uniaxial tensile test

The uniaxial tensile test is simulated to verify whether the exponential softening bond model can represent the whole stress-strain curve of concrete subjected to uniaxial tension. Huo et al. [28] developed a horizontal tensile test device and obtained the entire axial tensile stress-strain curve of concrete specimen with dimensions of  $100 \times 100 \times 550$  mm. As shown in Fig. 8, the spacing between two pre-embedded loading screws is 250 mm, so the effective loading length of the sample is 250 mm. The numerical specimen has a length of 290 mm which contains 20 mm of loading end on both sides. It is generated using the approach proposed by Potyondy and Cundall [15]. The radii of particles are distributed uniformly in the range from  $R_{\min}$  to  $R_{\max}$ , where  $R_{\min} = 1.0$  mm and  $R_{\max} = 1.6$  mm. After calibration, contact parameters are determined as follows:  $K_n = 32$  GPa,  $K_s = 16$  GPa,  $\sigma_t = 2.1$  MPa,  $\sigma_s = 2.1$  MPa,  $\mu = 0.5$ ,  $g_f = 40$  N/m, where  $\sigma_t$  and  $\sigma_s$  are tensile and shear strength in the form of stress, respectively. The input contact strength  $S_n$  and  $S_s$  are solved by  $2\bar{R}\sigma_t$  and  $2\bar{R}\sigma_s$ , respectively.

The loading process is controlled by displacement at a constant loading rate of 0.002 mm/min. The loading is terminated when the residual force is less than 1 % of the peak strength. As shown in Fig. 9, the simulated stress-displacement curve matches the experimental curves very well. Thus, the exponential softening bond model can well reflect the post-peak tensile softening behavior of the concrete.

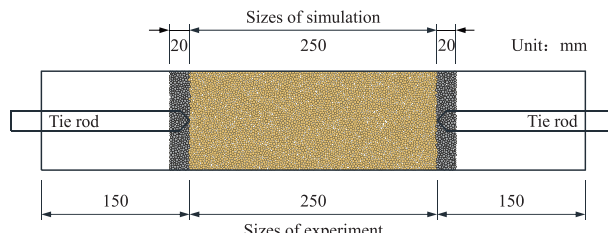


**Fig. 8.** Specimen and boundary conditions of the uniaxial tensile test.

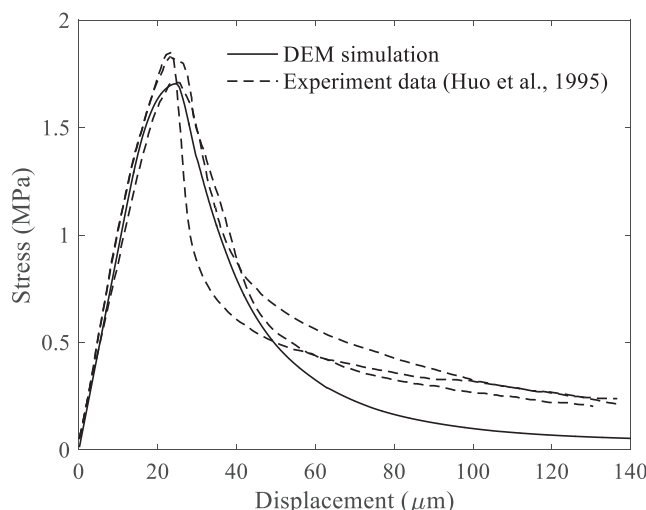


**Fig. 9.** Experimental and numerical load-displacement curves of the uniaxial tensile test.

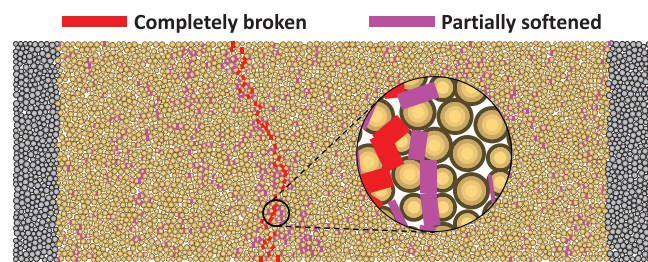


**Fig. 10.** The numerical micro cracks of specimen subjected to uniaxial tension at the end of loading.

In order to further verify the energy balance of the uniaxial tensile tests, the difference between macroscopic dissipated energy  $G_{macro}$  and microscopic fracture energy  $G_{micro}$  is analyzed.  $G_{macro} = W - U$ , where  $W$  is the external work, and  $U$  is the internal elastic strain energy of the sample.  $W$  equals the area enclosed by the uniaxial tensile force-displacement curve and the displacement axis, and  $U$  equals the sum of the elastic strain energy of all contacts.  $G_{micro}$  equals the sum of fracture energy dissipated by all contacts. As shown in Fig. 10, there are two kinds of softened contacts, i.e., completely broken contacts, and partially softened contacts. The energy dissipated by the completely broken contact is  $g_f \cdot \bar{R}t$ , and that dissipated by the partially softened contact must be determined according to its force-displacement relationship and damage state. The calculation results show that, at the end of loading, the external work  $W = 7.048$  N·m, and the elastic strain energy  $U = 0.191$  N·m, so the macroscopic dissipated energy is  $G_{macro} = 6.857$  N·m. The microscopic fracture energy  $G_{micro}$  is 6.862 N·m, and the difference between  $G_{micro}$  and  $G_{macro}$  is only 0.005 N·m. Thus, the consistency of these two dissipated energies further proves that the proposed contact model presents an excellent performance of fracture energy and can be used to simulate the fracture problems related to fracture energy.

### 3.3. Analysis of particle size dependency

Three-point bending fracture test was taken as an example to illustrate the impact of particle size on the fracture simulation results in DEM analysis. As shown in Fig. 11, the simulated sample has a height  $D$  of 100 mm, a width of 450 mm, a span  $S$  of 400 mm, an initial crack length  $a$  of 40 mm, and a thickness  $t$  of 13 mm.

Two bond models were used separately for comparison: the contact bond model and the exponential softening bond model. The same contact parameters are as follows:  $K_n = 19 \times 10^9$  N/m,  $K_s = 13.57 \times 10^9$  N/m,  $\sigma_t = 6$  MPa,  $\sigma_s = 12$  MPa,  $\mu = 0.5$ . The only difference between the two bond models is that the fracture energy  $g_f$  of the softening bond model is set to 61 N/m while cannot be set in the contact bond model. Three groups of simulations were performed using the average particle radius of 1 mm, 0.75 mm, and 0.5 mm, respectively, and the ratio of the maximum radius to the minimum radius is 1.6 in each group of simulations. Typical crack mouth opening displacement-load curves are shown in Fig. 12.

The crack mouth opening displacement-load curves simulated by the contact bond model show linear elastic deformations prior to the peak. When the contact stress at the crack tip exceeds the tensile strength, brittle fracture occurs, the contact force drops to 0, and the load on the structure also abruptly drops from its peak. Since the contact strength  $\sigma_t$  is the same for all cases, the load needed to break the first contact at the crack tip increases as the average particle size increases. As a result, the peak load shows an increasing trend with the increasing particle size. Therefore,

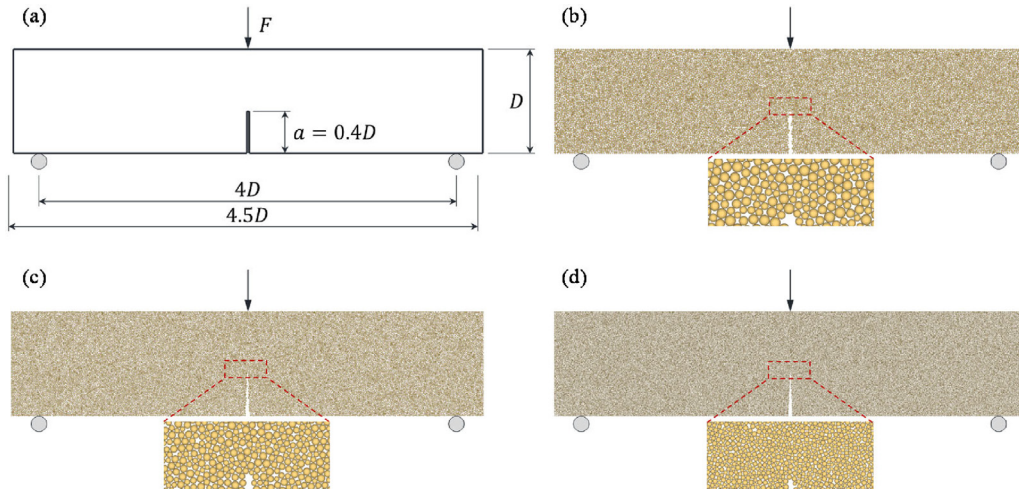


**Fig. 11.** The sketch and some typical specimens of the three-point bending fracture tests. (a) Sketch of three-point bending fracture test, (b) a specimen with the average particle radius of 1 mm, (c) a specimen with the average particle radius of 0.75 mm, and (d) a specimen with the average particle radius of 0.5 mm.

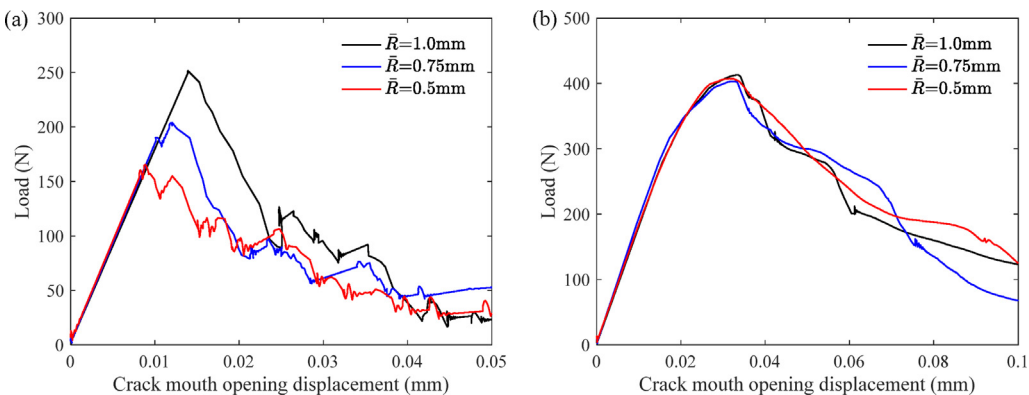


**Fig. 12.** Crack mouth opening displacement-force curves of three-point bending tests simulated by (a) the contact bond model and (b) the exponential softening bond model.

the contact bond model exhibits an obvious particle size dependency.

While the crack mouth opening displacement-load curves simulated by the exponential softening bond model are almost the same, and the particle size dependency is eliminated. After the contact stress at the crack tip exceeds the tensile strength, the contact force will not drop to zero but gradually decreases under the influence of the exponential softening bond. As a result, the load on the structure will keep increasing, and the crack opening displacement-load curve has an obvious yield stage before the peak. Therefore, the peak load simulated by the softening bond is larger than that simulated by the contact bond under the same conditions of particle size and strength parameters. Since the fracture energy remains constant and does not vary with particle size, the energy required for crack propagation and the elastic strain energy of the structure are not affected by particle size. According to the energy conservation law, the external works simulated by various particle sizes are almost equal, which means that the areas enclosed by the load-displacement curves and the displacement axes are approximately identical. Therefore, the crack mouth opening displacement-load curves and peak loads simulated by different particle sizes are nearly identical.

Potyondy and Cundall [15] analyzed the size dependency of the brittle bond model based on linear elastic fracture mechanics (LEFM), and they found that the fracture toughness  $K_{IC}$ , and the

average particle size  $\bar{R}$  in DEM simulation have the following relationship:

$$K_{IC} = \sigma_t \sqrt{\pi \alpha \bar{R}} \quad (18)$$

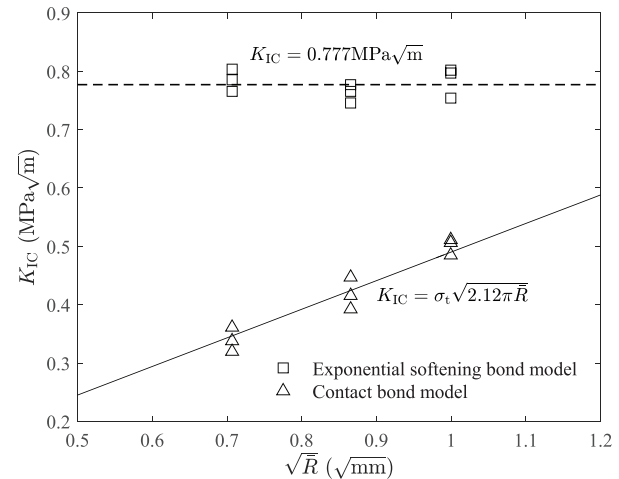


**Fig. 13.** The influence of particle size on the simulation results of fracture toughness.

where  $\sigma_t$  is the tensile strength of bond,  $\alpha$  is a dimensionless factor reflecting the random distribution of particles, and  $\alpha \geq 1$ .

According to a handbook [29], the fracture toughness of three points bending specimen analyzed in this study is:

$$K_{IC} = \frac{6F_{max}\sqrt{\alpha}}{t\sqrt{D}} \frac{1.99 - \alpha(1-\alpha)(2.15 - 3.93\alpha + 2.7\alpha^2)}{(1+2\alpha)(1-\alpha)^{3/2}} \quad (19)$$

where  $\alpha = a/D$  and  $F_{max}$  is the peak load.

The mode I fracture toughness calculated by the simulated peak load is shown in Fig. 13. With the increase of the average radius, the fracture toughness obtained by the exponential softening bond model remains constant at about  $0.777 \text{ MPa}\sqrt{m}$ . However, the fracture toughness obtained by the contact bond model presents an increasing trend and is linearly related to the square root of the average particle size. This result is consistent with Eq. (18), where the coefficient  $\alpha$  is about 2.12.

Therefore, the contact bond model presents an obvious particle size dependency, regardless of the theoretical formula or the simulation results. Under the condition of the same strength parameters, the simulation with a smaller particle size could result in a smaller fracture toughness. When the contact bond model is used to simulate the fracture characteristics of a material, the average particle radius should be solved in advance by substituting the material's fracture toughness into Eq. (18). However, the calculated particle size may be too large to conduct fracture simulation on a small specimen. For example, the material simulated in this section has a fracture toughness of  $0.777 \text{ MPa}\sqrt{m}$ , and the calculated particle size  $\bar{R}$  is about 2.5 mm. When this particle size is used for the fracture analysis of a specimen smaller than 100 mm, the number of particles is not enough to guarantee the accuracy of the simulation result.

In contrast, the proposed softening bonding model takes fracture energy as an important parameter to adjust the post-peak contact deformation behavior. By this strategy of fracture energy regularization, the proposed model eliminates the particle size dependency of fracture simulation results in DEM. It facilitates the selection of particle size in discrete element analysis and ensures the reliability of fracture analysis. Although the proposed softening bonding model is verified and analyzed with circular particles, it could also work in the cases of poly-dispersed particle assemblies as well as polygonal particles by assigning the proposed model to their boundary contacts.

#### 4. Size effect analysis of mode I fracture

Bažant et al. [30] performed three-point bending fracture tests on similar limestone specimens of various sizes to investigate the size effect of Mode I fracture. The experimental data are cited here to conduct numerical simulations.

##### 4.1. Microscopic mechanical parameters of limestone

The limestone has a density of  $2200 \text{ kg/m}^3$ , an elastic modulus of  $15.3 \text{ GPa}$ , a Poisson ratio of 0.15, a Brazilian split tensile strength of  $3.45 \text{ MPa}$ , and a fracture energy of  $61 \text{ N/m}$ . By taking these macro properties as the targets, uniaxial compression and Brazilian splitting tests were simulated to calibrate the microscopic parameters of discrete elements. For comparison, the following simulations were conducted using the contact bond model [27], the linear softening bond model [27], and the exponential softening bond model, respectively. The calibrated macro properties of limestone are shown in Table 2. All three bond models can well reflect the elastic modulus, the Poisson ratio, and the Brazilian splitting tensile strength of the limestone. The microscopic parameters shown in Table 3 were calibrated according to these macro properties and were used for the following simulations. For the linear and exponential softening bond models, the fracture energy is input as a parameter to eliminate particle size dependency.

##### 4.2. Simulation of three-point bending test

The sketch of the three-point bending fracture test investigated by Bažant et al. [30] is shown in Fig. 11(a). Four groups of similar specimens were modeled. The heights  $D$  of these numerical specimens are 12.7, 25.4, 50.8, and 101.6 mm, respectively, and the thicknesses of these specimens are 13 mm. The rest dimensions meet the proportions shown in Fig. 11(a). Three specimens were simulated for each group. Since the strategy of fracture energy regularization can eliminate the particle size dependency of numerical results, the average radius  $\bar{R}$  was set to  $D/150$  in the analyses of the softening models. While the average radius  $\bar{R}$  was set to 0.05 mm in the analyses of the contact bond model. The crack mouth opening displacement and load were monitored during the calculation process.

The simulated crack mouth opening displacement-load curves are compared with the experimental results, as shown in Fig. 14.

**Table 2**  
Experimental and simulated macro properties of limestone.

Models	Elastic modulus $E(\text{GPa})$	Poisson ratio $\nu$	Brazilian split tensile strength $f_t(\text{MPa})$	Uniaxial compressive strength $\sigma_c(\text{MPa})$
Experiments	15.3	0.15	3.45	-*
Contact bond	15.33	0.14	3.45	14.29
Linear softening bond	15.22	0.15	3.46	15.86
Exponential softening bond	15.21	0.15	3.44	15.41

\* Uniaxial compressive strength is not tested in the literature.

**Table 3**  
Micro parameters of limestone in DEM.

Models	Normal contact stiffness $K_n(\text{N/m})$	Shear contact stiffness $K_s(\text{N/m})$	Normal bond strength $\sigma_t(\text{MPa})$	Shear bond strength $\sigma_s(\text{MPa})$	Friction coefficient $\mu$	Fracture energy $g_f(\text{N/m})$
Contact bond	$19 \times 10^9$	$13.57 \times 10^9$	7.9	15.8	0.5	-
Linear softening bond	$19 \times 10^9$	$13.57 \times 10^9$	4.0	8.0	0.5	61.0
Exponential softening bond	$19 \times 10^9$	$13.57 \times 10^9$	6.0	12.0	0.5	61.0

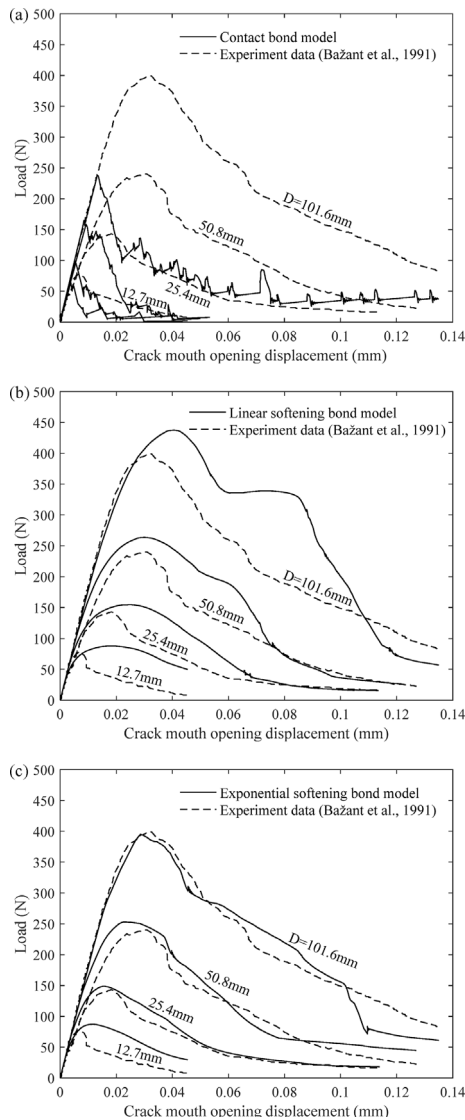


**Fig. 14.** Typical crack mouth opening displacement-load curves of three-point bending tests simulated by (a) the contact bond model, (b) the linear softening bond model, and (c) the exponential softening bond model.

**Table 4**  
Peak loads of the three-point bending fracture tests.

Height of samples <i>D</i> (mm)	Peak load $F_{\max}$ (N)			
	Experiment	Contact bond	Linear softening bond	Exponential softening bond
12.7	82	59.1	87.8	87.2
	85	60.1	94.4	84.0
	78	64.2	89.2	86.0
25.4	134	94.5	154.8	148.8
	140	96.3	166.1	143.8
	140	101.9	159.2	147.1
50.8	238	158.8	263.6	253.0
	243	152.9	287.0	237.8
	243	149.8	276.7	247.0
101.6	418	245.5	437.4	395.2
	405	228.2	473.1	368.6
	394	239.2	466.9	410.5
Average error	0.0	79.1	29.7	7.9

The numerical results show that all three bond models match the experimental curves very well in the pre-peak deformation stage. However, the results simulated by the exponential softening bond model show a better representation of the post-peak deformation characteristics than those simulated by the other two bond models. Therefore, the post-peak stress-strain relationship of limestone is more likely to be exponential softening when subjected to tensile loading.

The peak loads obtained by both the experiments and the simulations are listed in Table 4. The differences between the numerical results and the experimental results are compared. Compared with the peak loads obtained by the exponential softening bond model, those obtained by the contact bond model are smaller, and those obtained by the linear softening bond model are larger. The simulated peak load is mainly related to the fracture energy of bonds. According to the contact force-displacement relationship, when the contact bond breaks, the dissipated fracture energy is 1.64 N/m. Since it is less than the fracture energy of limestone, which is 61 N/m, the external load needed for crack propagation is also smaller. Although the fracture energy of the linear softening bond is set to 61 N/m, its fracture energy dissipation process is different from that of the exponential softening bond model. In the early stages of damage, the fracture energy dissipated rate of the linear softening bond model is less than that of the exponential softening bond model, so the linear softening bond requires a larger peak load to break limestone.

The average errors of the peak loads are further used to assess the accuracy of the numerical results. Table 4 shows that the average errors of the peak loads simulated by the contact bond model, the linear softening bond model, and the exponential softening bond model are 79.1, 29.7, and 7.9 N, respectively. Thus, the exponential softening bond model presents a higher simulation accuracy.

#### 4.3. Size effect analysis of mode I fracture

Bažant et al. [30] compared the experimental peak loads with their size effect law, which is expressed as:

$$\sigma_N = \frac{Bf_t}{\sqrt{1 + D/D_0}} \quad (20)$$

where  $B$  and  $D_0$  are two parameters of the size effect law,  $f_t$  is the Brazilian split tensile strength, and  $\sigma_N$  is nominal strength of fracture structure.  $\sigma_N$  can be calculated as:

$$\sigma_N = c_n \frac{F_{\max}}{Dt} \quad (21)$$

where  $c_n$  is an arbitrary dimensionless coefficient and can be valued according to structural characteristics. For the three-point bending structure analyzed in this study,  $c_n=1$ .

Using the size effect law, Bažant et al. [30] fitted the experimental data of nominal strength, and the fitting parameters are as follows:  $B = 0.156$  and  $D_0 = 51.6$  mm. The theoretical size effect curve is shown in Fig. 15. In order to analyze the differences between the numerical results and the experimental data, it is more reasonable to present the numerical nominal strengths in the figure by adopting the fitting parameters of the experimental data instead of fit-

ting a new set of parameters for each group of simulations. When all the simulation data are presented with the same fitting parameters, the distance between the simulation data and the theoretical curve indicates the simulation's accuracy. It is found that the numerical data simulated by the exponential softening bond model are closer to the theoretical curve. The numerical data simulated by the linear softening bond are roughly parallel to the theoretical curve, but the distance is larger. The data points simulated by the contact bond model are far from the theoretical curve, so it cannot reflect the size effect law of the simulated specimens. Therefore, the exponential softening bond model is the most accurate method among these three models to represent the size effect of limestone.

#### 4.4. Characteristics of fracture process zone

As the specimen height increases, the failure mode changes from ductile failure to brittle failure. And this transformation is closely related to the size of the fracture process zone relative to the structural size. Fig. 16 shows the cracks and fracture process zones of various specimens with different heights under the condition of peak load. There are two kinds of cracks, i.e., completely broken cracks marked as red lines and partially softened cracks marked as magenta lines. The cracks simulated by the contact bond are completely separated, and the relative length of the extended crack,  $L_c/D$ , does not change too much as the specimen height increases, so these specimens present the characteristics of brittle fracture. However, the specimens simulated by the linear and exponential softening models do not generate any completely broken cracks yet under the condition of peak load. Instead, the cracks are partially softened cracks and initiate in a damaged band known as the fracture process zone. As the specimen height increases, the relative length of the fracture process zone,  $L_p/D$ , gradually decreases, so the failure mode transforms from ductile failure to brittle failure. The simulation results of the exponential softening model present a more noticeable change in the relative length of the fracture process zone than those of the linear softening model,

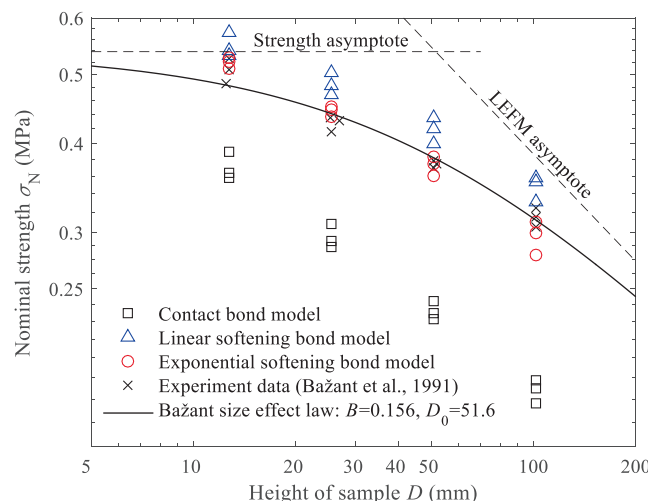


Fig. 15. The experimental and numerical results of size effect.

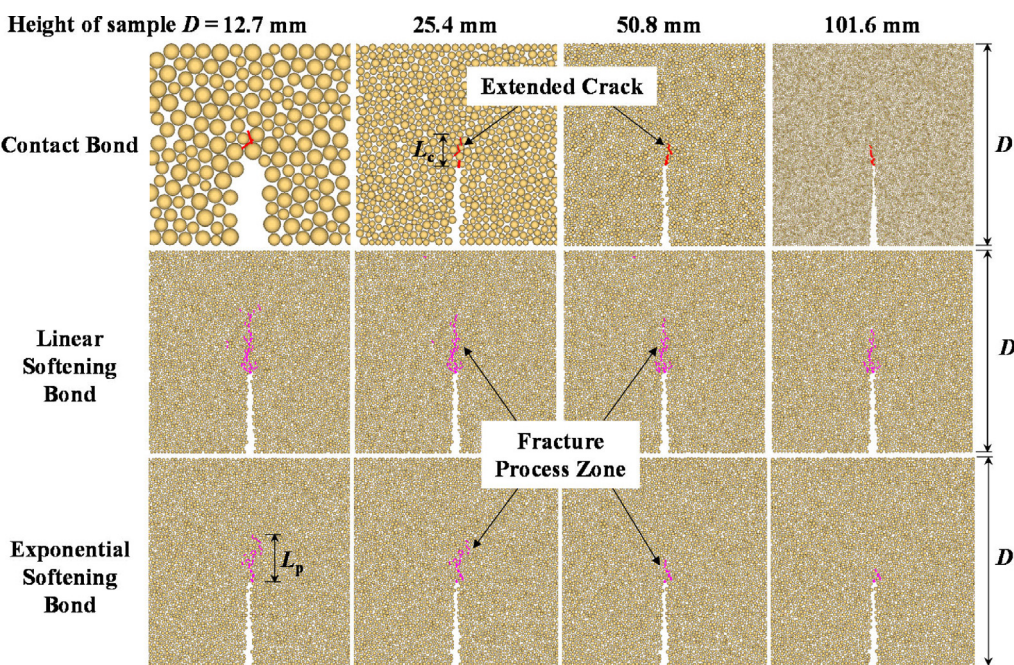


Fig. 16. Cracks and fracture process zones of various specimens under the condition of peak load.

which means that the exponential softening model represents the transition of failure mode better.

## 5. Conclusion

This study develops an energy-balanced exponential softening bond model in DEM to solve the problem that the current contact models cannot effectively represent the size effect of Mode I fracture. The proposed model is analyzed and validated in terms of fracture energy and size effect by some simulations of fracture tests. The main conclusions are as follows:

- (1) The constitutive relationship of the exponential softening bond model is established based on an exponential damage law and an elliptic yield criterion. The exponential damage law describes the softening process of tensile strength and shear strength. And the elliptic yield criterion ensures that the total fracture energy of the normal and shear springs always equals the fracture energy of the resultant contact force.
- (2) The fracture simulation of the contact bond model exhibits significant particle size dependency, that the simulated fracture toughness is proportional to the square root of particle radius. This particle size dependency can be effectively eliminated by adjusting the force-displacement relationship of a softening bond model based on fracture energy and particle size. The elimination of particle size dependency facilitates the selection of particle radius and ensures the validity of fracture simulation results.
- (3) The exponential softening bond model can effectively simulate the whole stress-strain curve of concrete subjected to uniaxial tensile load. The simulation result of the uniaxial tensile test also demonstrates that the work done by the external force is equal to the sum of microscopic elastic strain energy and fracture energy, so the energy balance can be accurately reflected by the proposed model.
- (4) The contact bond model, the linear softening bond model, and the exponential softening bond model were used to simulate the size effect of three-point bending fracture tests of a limestone. Compared with the contact bond model, softening bond models can more effectively represent the size effect of Mode I fracture. The simulated results of the exponential softening bond model, including the load-displacement curve, peak load, and size effect, are closer to the experimental results than those of the linear softening bond model, so it represents the traction-separation relationship of limestone better.

## Data availability

Data will be made available on request.

## Declaration of Competing Interest

The authors declare that they have no known competing financial interests or personal relationships that could have appeared to influence the work reported in this paper.

## Acknowledgements

This study was financially supported by the National Natural Science Foundation of China (No. 52109135) and the China Postdoctoral Science Foundation General Program (No. 2019M653402). We gratefully acknowledge the aforementioned supports.

## References

- [1] Bažant ZP. Size Effect in Blunt Fracture: Concrete, Rock. *Metal J Eng Mech* 1984;110(4):518–35. [https://doi.org/10.1061/\(ASCE\)0733-9399\(1984\)110:4\(518\)](https://doi.org/10.1061/(ASCE)0733-9399(1984)110:4(518)).
- [2] Ayatollahi MR, Akbaroost J. Size and Geometry Effects on Rock Fracture Toughness: Mode I Fracture. *Rock Mech Rock Eng* 2014;47(2):677–87. <https://doi.org/10.1007/s00603-013-0430-7>.
- [3] Usoltseva OM, Tsoi PA. The Influence of Size Effect on Strength and Deformation Characteristics of Different Types of Rock Samples. *IOP Conference Series: Earth and Environmental Science* 2021;720(1):12089. 10.1088/1755-1315/720/1/012089.
- [4] Griffith AA. The phenomena of rupture and flow in solids. *Phil Trans R Soc Lond A* 1921;221(582–593):163–98. <https://doi.org/10.1098/rsta.1921.0006>.
- [5] Weibull W. A Statistical Distribution Function of Wide Applicability. *J Appl Mech* 1951;18(3):293–7. <https://doi.org/10.1115/1.4010337>.
- [6] Bažant ZP, Oh BH. Crack band theory for fracture of concrete. *Mat Constr* 1983;16(3):155–77. <https://doi.org/10.1007/BF02486267>.
- [7] Hillerborg A, Modéer M, Petersson P-E. Analysis of crack formation and crack growth in concrete by means of fracture mechanics and finite elements. *Cem Concr Res* 1976;6(6):773–81. [https://doi.org/10.1016/0008-8846\(76\)90007-7](https://doi.org/10.1016/0008-8846(76)90007-7).
- [8] Scamardo M, Franchi A, Crespi P. A non-standard numerical method for finite element modelling of tensile cracks in quasi-brittle material. *Comput Struct* 2022;258(5). <https://doi.org/10.1016/j.compstruc.2021.106664>.
- [9] Nemes JA, Spéciel E. Use of a rate-dependent continuum damage model to describe strain-softening in laminated composites. *Comput Struct* 1996;58(6):1083–92. [https://doi.org/10.1016/0045-7949\(95\)00229-4](https://doi.org/10.1016/0045-7949(95)00229-4).
- [10] Bažant ZP, Planas J. *Fracture and Size Effect in Concrete and Other Quasibrittle Materials*. Routledge; 2019.
- [11] Yun K, Wang Z, Chang M, Liu J, Kim T-J, Son N, et al. A computational methodology for simulating quasi-brittle fracture problems. *Comput Struct* 2019;215(1):65–79. <https://doi.org/10.1016/j.compstruc.2019.02.003>.
- [12] Minh NH, Cheng YP. A DEM investigation of the effect of particle-size distribution on one-dimensional compression. *Géotechnique* 2013;63(1):44–53. <https://doi.org/10.1680/geot.10.P.058>.
- [13] Yang B, Jiao Y, Lei S. A study on the effects of microparameters on macroproperties for specimens created by bonded particles. *Eng Comput* 2006;23(6):607–31. <https://doi.org/10.1108/02644400610680333>.
- [14] Schlangen E, van Mier JGM. Simple lattice model for numerical simulation of fracture of concrete materials and structures. *Mater Struct* 1992;25(9):534–42. <https://doi.org/10.1007/BF02472449>.
- [15] Potyondy DO, Cundall PA. A bonded-particle model for rock. *Int J Rock Mech Min Sci* 2004;41(8):1329–64. <https://doi.org/10.1016/j.ijrmms.2004.09.011>.
- [16] Jirásek M, Bauer M. Numerical aspects of the crack band approach. *Comput Struct* 2012;110–111:60–78. <https://doi.org/10.1016/j.compstruc.2012.06.006>.
- [17] Vogel A, Junker P. Adaptive and highly accurate numerical treatment for a gradient-enhanced brittle damage model. *Int J Numer Methods Eng* 2020;121(14):3108–31. <https://doi.org/10.1002/nme.6349>.
- [18] Havlásek P, Grassl P, Jirásek M. Analysis of size effect on strength of quasi-brittle materials using integral-type nonlocal models. *Eng Fract Mech* 2016;157:72–85. <https://doi.org/10.1016/j.engfracmech.2016.02.029>.
- [19] Feng D-C, Wu J-Y. Phase-field regularized cohesive zone model (CZM) and size effect of concrete. *Eng Fract Mech* 2018;197(4):66–79. <https://doi.org/10.1016/j.engfracmech.2018.04.038>.
- [20] Liakas S, O'Sullivan C, Saroglou C. Influence of heterogeneity on rock strength and stiffness using discrete element method and parallel bond model. *J Rock Mech Geotech Eng* 2017;9(4):575–84. <https://doi.org/10.1016/j.jrmge.2017.02.003>.
- [21] Kim H, Buttlar WG. Discrete fracture modeling of asphalt concrete. *Int J Solids Struct* 2009;46(13):2593–604. <https://doi.org/10.1016/j.ijsolstr.2009.02.006>.
- [22] Kim H, Wagoner MP, Buttlar WG. Simulation of Fracture Behavior in Asphalt Concrete Using a Heterogeneous Cohesive Zone Discrete Element Model. *J Mater Civ Eng* 2008;20(8):552–63. [https://doi.org/10.1061/\(ASCE\)0899-1561\(2008\)20:8\(552\)](https://doi.org/10.1061/(ASCE)0899-1561(2008)20:8(552)).
- [23] Kim H, Wagoner MP, Buttlar WG. Micromechanical fracture modeling of asphalt concrete using a single-edge notched beam test. *Mat Constr* 2009;42(5):677–89. <https://doi.org/10.1617/s11527-008-9412-8>.
- [24] Fakhimi A, Tarokh A. Process zone and size effect in fracture testing of rock. *Int J Rock Mech Min Sci* 2013;60(3):95–102. <https://doi.org/10.1016/j.ijrmms.2012.12.044>.
- [25] Nooru-Mohamed MB. *Mixed-mode fracture of concrete: An experimental approach*. PhD Thesis 1992.
- [26] Bobiński J, Tejchman J. Comparison of continuous and discontinuous constitutive models to simulate concrete behaviour under mixed-mode failure conditions. *Int J Numer Anal Meth Geomech* 2016;40(3):406–35. <https://doi.org/10.1002/nag.2411>.
- [27] Itasca Consulting Group Inc. *PFC2D (Particle Flow Code in 2 Dimensions) User's Guide*. 4th ed. USA: Minnesota; 2008.
- [28] Huo H, Che L, Liang Z. Test and equipment of concrete axial tension complete stress-strain curve. *J Hohai Univ* 1995;23(5):26–31. in Chinese.
- [29] Tada H, Paris PC, Irwin GR. *The Stress Analysis of Cracks Handbook*. Third Edition. ASME Press; 2000.
- [30] Bažant ZP, Gettu R, Kazemi MT. Identification of nonlinear fracture properties from size effect tests and structural analysis based on geometry-dependent R-curves. *International Journal of Rock Mechanics and Mining Sciences & Geomechanics Abstracts* 1991;28(1):43–51. [https://doi.org/10.1016/0148-9062\(91\)93232-U](https://doi.org/10.1016/0148-9062(91)93232-U).